Acta Crystallographica Section A
Foundations of Crystallography
ISSN 0108-7673

Received 1 February 2013
Accepted 9 July 2013

One-step model of the face-centred-cubic to body-centred-cubic martensitic transformation

Cyril Cayron

CEA, LITEN, 17 rue des Martyrs, Grenoble 38054, France. Correspondence e-mail: cyril.cayron@cea.fr

A 'one-step' theory based on Pitsch distortion is proposed to explain the continuity between the orientations of the Kurdjumov–Sachs (KS), Nishiyama–Wassermann (NW) and Pitsch variants observed on the electron backscatter diffraction pole figures of martensitic alloys. The Pitsch distortion respects the hard-sphere packing of the iron atoms and implies the existence of a neutral line along the close-packed direction $[110]_\gamma = [111]_\alpha$. Its principal strains are 0, −5.7 and 15.5%, well below the +12, +12 and −20% values of the Bain distortion. At the nucleation step, the distortion generates martensite that continuously deforms the austenitic matrix. Martensite continues to grow in Pitsch orientation inside the deformation field of the surrounding austenite to reach KS and NW orientations in reference to the bulk austenite. Some experimental results reported in the literature are revisited, such as the $\{225\}_\gamma$ habit planes, the sometimes observed 'twins' at the midrib, the formation of butterfly martensite, and the effect of prior plastic deformation of austenite on the transformation temperature and on variant selection mechanisms.

1. Introduction

Martensite, generally noted α', or here simply α, is a body-centred cubic (b.c.c.) or body-centred tetragonal (b.c.t.) metastable hard phase obtained in steels and other iron alloys by rapid cooling of the high-temperature face-centred cubic (f.c.c.) phase, the austenite γ. Many orientation relationships (ORs) between the α martensitic variants and the γ parent grains are reported in the literature (Table 1). KS ORs (Kurdjumow & Sachs, 1930) and NW ORs (Nishiyama, 1934; Wassermann, 1933) were measured by X-ray diffraction; GT ORs (Greninger & Troiano, 1949) and Pitsch ORs (Pitsch, 1959) were identified by transmission electron microscopy (TEM) diffraction. More recently, a precise average OR was also determined by Miyamoto *et al.* (2009) by electron backscatter diffraction (EBSD). The Bain OR was considered by Bain (1924) as the result of a distortion composed of a compression of 20% along the $[001]_\gamma$ axis and an expansion of 12% along the $[110]_\gamma$ and $[\bar{1}10]_\gamma$ axes. However, the Bain OR is more than 10° away from the experimentally determined KS, NW or GT ORs. The KS is the most often reported OR. The Pitsch and NW are two complementary ORs (the indices γ and α are interchanged). The NW and Pitsch ORs are both 5° away from the KS OR (Dahmen, 1982).

The main crystallographic models of martensitic transformation are (*a*) the Bain distortion, (*b*) the Kurdjumov–Sachs–Nishiyama (KSN) shear/dilatation model, and (*c*) the Bogers & Burgers (BB) model, later refined by Olson & Cohen (OC) (a brief description and references are given in Supplementary Material 1[1]). None of these models seems to be totally satisfactory. The high-resolution transmission electron microscopy (HRTEM) investigations of Kajiwara *et al.* (1996) and Ogawa & Kajiwara (2007) on the structure of the austenite/martensite interfaces invalidate the BB model, and seem to agree with the KSN model. Interestingly, Sandoval *et al.* (2009) recently showed by atomistic simulations that the KSN path is energetically more favourable than the Bain path. However, the KSN model is far from the consensus due to its large atomic displacements and strains. Sinclair & Hoagland (2008) showed by molecular-dynamics simulations that the OC model can provide sufficient conditions for the nucleation of α martensite, and found that the α nuclei are actually in the Pitsch OR with the surrounding austenite. Since the most representative OR in steels is KS, the authors raised some questions about the validity of the OC model. Sinclair (2010) showed later that the α martensite can be formed at the intersection of hexagonal-close-packed (h.c.p.) ε bands and noticed that the rapid increase in growth kinetics corresponds to a change in the orientation relationship from the Pitsch OR to the KS OR.

The phenomenological theory of martensite transformation (PTMT) developed in the 1950s is actually the classical model of martensitic transformation (see Supplementary Material 2).

[1] Supplementary documents describing (1) some crystallographic models of martensitic transformation, (2) the effect of the EBSD step size on the pole figures of martensitic variants, (3) the use of a groupoid composition table to define crystallographic packets of martensitic variants in the Kurdjumov–Sachs orientation relationship, (4) Pitsch rotations A and B, disclinations and dislocations, and (5) the effect of plastic deformation of austenite are available from the IUCr electronic archives (Reference: PC5027). Services for accessing this material are described at the back of the journal.

Table 1
Different orientation relationships for martensite reported in the literature.

References and abbreviations are Bain (1924), KS = Kurdjumov–Sachs (Kurdjumow & Sachs, 1930), GT = Greninger–Troiano (Greninger & Troiano, 1949), NW = Nishiyama (1934)–Wassermann (1933), and Pitsch (1959).

Name	Orientation relationship
Bain	$(001)_\gamma$ // $(001)_\alpha$ and $[110]_\gamma$ // $[100]_\alpha$
KS	$(111)_\gamma$ // $(110)_\alpha$ and $[\bar{1}10]_\gamma$ // $[\bar{1}11]_\alpha$
GT	$(111)_\gamma$ // $(110)_\alpha$ (at 1°) and $[\bar{1}\bar{2},17,\bar{5}]_\gamma$ // $[\bar{1}\bar{7},17,7]_\alpha$
NW	$(111)_\gamma$ // $(110)_\alpha$, $[\bar{1}10]_\gamma$ // $[001]_\alpha$, $[11\bar{2}]_\gamma$ // $[\bar{1}10]_\alpha$
Pitsch	$(110)_\gamma$ // $(111)_\alpha$, $[001]_\gamma$ // $[\bar{1}10]_\alpha$, $[\bar{1}10]_\gamma$ // $[11\bar{2}]_\alpha$

It brings together the Bain distortion, the observed ORs and the habit planes (HPs) in the same mathematical approach. However, contrary to the crystallographic models mentioned above, the exact atomic displacements of the iron atoms during the transformation are beyond its scope.

In parallel with these works, we developed a method to reconstruct the prior austenitic grains from EBSD maps (Cayron *et al.*, 2006; Cayron, 2006, 2007*b*) and it was observed that the pole figures of the martensite grains inside the prior

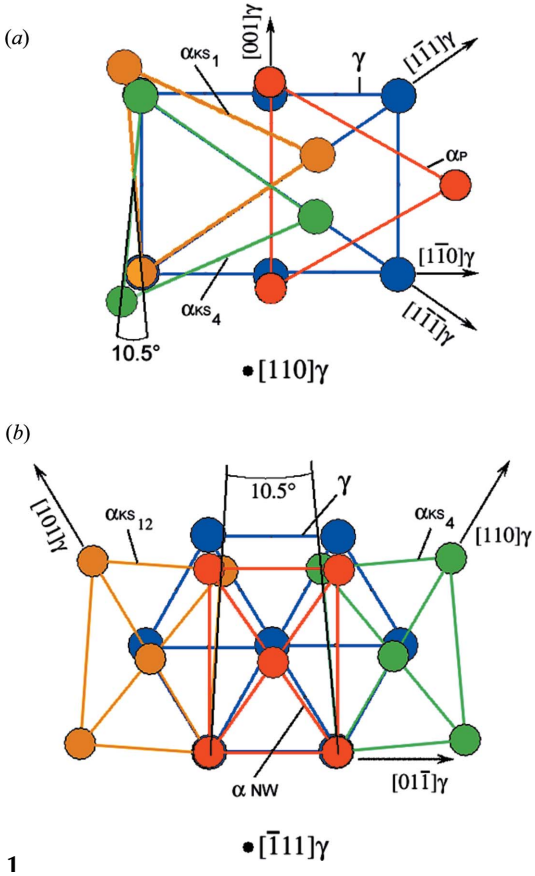

Figure 1
Representation in direct space of the low-misorientation operators. (*a*) Operator 2A with γ oriented along the $[110]_\gamma$ // $[111]_\alpha$ direction. The KS α_1 and α_4 variants are in green and in yellow, respectively, and the Pitsch variant in mid-orientation in red. (*b*) Operator 2B with γ oriented along the $[\bar{1}11]_\gamma$ // $[110]_\alpha$ direction. The KS α_4 and α_{12} variants are in green and yellow, respectively, and the NW variant in mid-orientation in red.

austenitic grains showed continuum paths between the KS and NW ORs. These paths were simulated with two continuous rotations A(*a*) and B(*b*), which were considered as traces of the transformation mechanism, and a 'two-step' theory of martensitic transformation was proposed (Cayron *et al.*, 2010). That theory foresees the existence of an intermediate h.c.p. ε phase in all the b.c.c. martensitic steels (even if only fleeting). This model can be considered as a KSN shear helped by Shockley partial dislocations. However, in spite of its physical base, the 'two-step' model cannot easily explain the large variety of morphologies and HPs. Indeed, the first f.c.c.–h.c.p. step should produce plates on the $(111)_\gamma$ planes and the next h.c.p.–b.c.c. step should give other plates or needles inside the first plates, as actually observed in FeMn alloys in which the ε phase is a stable phase (Shimizu & Tanaka, 1978). Moreover, the fact that continuous features are observed in the EBSD pole figures of many iron alloys, whatever their composition and the heat treatment and whatever the morphology and HPs, leads us to consider them as the trace of a unique mechanism, and not as two unrelated ones.

The aim of this paper is to present a 'one-step' model in which rotations A(*a*) and B(*b*) are correlated. They will be shown to be a consequence of the same unique mechanism based on Pitsch distortion. In §2, the continuous features in the EBSD pole figures are re-investigated. The Pitsch distortion, which is described in §3, is shown to be in agreement with the EBSD pole figures in §4. Some observations reported in the literature are discussed with the 'one-step' model in §5. The model is qualitative and mainly aims to explain the orientation gradients at the mesoscale. The structure and configuration of dislocations in the interfaces, as treated in the topological model of Pond *et al.* (2008), will not be discussed.

2. Continuous features in EBSD pole figures

The EBSD pole figures of the orientations of the martensite variants that belong to the same prior-austenitic grains exhibit continuous features (the EBSD step size should be adjusted to obtain more than 1000 pixels per lath, as shown in Supplementary Material 2). In a previous paper (Cayron *et al.*, 2010) these features were simulated by using the KS variants and the rotations A(*a*) around $\langle 111\rangle_\alpha$ // $\langle 110\rangle_\gamma$ of angle *a* varying between 0 and +10°, and the rotations B(*b*) around $\langle 110\rangle_\alpha$ // $\langle 111\rangle_\gamma$ of angle *b* varying between 0 and 6°. However, the KS, NW and Pitsch variants can be linked by limiting the angles of rotations *a* and *b* to only 5.26°. Indeed, let us consider the 24 KS variants; they can be grouped by using three special crystallographic packets: the close-packed plane (CPP) packet, the close-packed direction (CPD) packet and the Bain packet. There are two low-angle misorientations between the KS variants: the rotation A(10.5°) = 10.5°/$[111]_\alpha$ and B(10.5°) = 10.5°/$[110]_\alpha$, named 2A and 2B, respectively. The operator 2A links the low-misoriented KS variants in the CPD packets, and the operator 2B links the low-misoriented KS variants in the CPP packets. The rigorous algebraic definition of packets and operators, as well as the indices of variants that are used in this paper, are given in Supplementary Material 3.

The Pitsch variants are on the CPD packets at the mid-positions between the pairs of KS variants linked by the operator 2A. Each Pitsch variant is linked to a KS variant by an operator A represented by a rotation of angle $a_{\max} = 10.5^\circ/2$. Since the angular value of 10.5° of the operator 2A results from the distortion of the 70.5° angle of the $\langle 111\rangle_\gamma$ directions in the $(110)_\gamma$ plane into the 60° angle of the $\langle 110\rangle_\alpha$ directions in the $(111)_\alpha$ // $(110)_\gamma$ plane (Fig. 1*a*), the angle between the Pitsch variants and the KS variants of the pair is precisely

$$\begin{aligned} a_{\max} &= \tfrac{1}{2}[\arccos(1/3) - \arccos(1/2)] \\ &= \tfrac{1}{2}\arccos(\sqrt{2/3} + 1/6) \\ &\approx 5.26^\circ. \end{aligned} \quad (1)$$

The NW variants are on the CPP packets at the mid-positions between the pairs of KS variants linked by the operator 2B. Each NW variant is linked to a KS variant of the pair by a operator B represented by a rotation of angle $b_{\max} = 10.5^\circ/2$. Since the angular value of 10.5° of the operator 2B results from the distortion of the 60° angle of the $\langle 110\rangle_\gamma$ directions in the $(\bar{1}11)_\gamma$ plane into the 70.5° angle of the $\langle 111\rangle_\alpha$ directions in the $(110)_\alpha$ // $(\bar{1}11)_\gamma$ plane (Fig. 1*b*), the angle between the NW variants and the KS variants of the pair is precisely

$$\begin{aligned} b_{\max} &= \tfrac{1}{2}[\arccos(1/3) - \arccos(1/2)] \\ &= \tfrac{1}{2}\arccos(\sqrt{2/3} + 1/6) \\ &\approx 5.26^\circ. \end{aligned} \quad (2)$$

This analysis shows that the continuous rotations A(a) and B(b) acting on the 24 KS variants, with a varying between 0 and 5.26° and b varying between 0 and 5.26°, are sufficient to create the continuum of orientations and make the pole figure a closed structure. Rotation A closes the $\langle 111\rangle_\alpha$ CPDs *via* the 12 Pitsch variants, and rotation B closes the $\{110\}_\alpha$ CPPs *via* the NW variants. The pole figures have been simulated, as done by Cayron *et al.* (2010), but now by limiting the maximum value of angles a and b to 5.26°, and they continue to be in good agreement with experimental pole figures[2] (Fig. 2). The fit could even be slightly improved by combining the rotations A and B, *i.e.* by introducing the continuous rotation A(c) + B(5.26° − c) with $c \in [0, 5.26^\circ]$.

[2] The part generated by A(a) with a between 5.26 and 10.5° in Cayron *et al.* (2010) was actually overlapped by the part generated by A(a) with a between 0 and 5.26°, and was unnecessary.

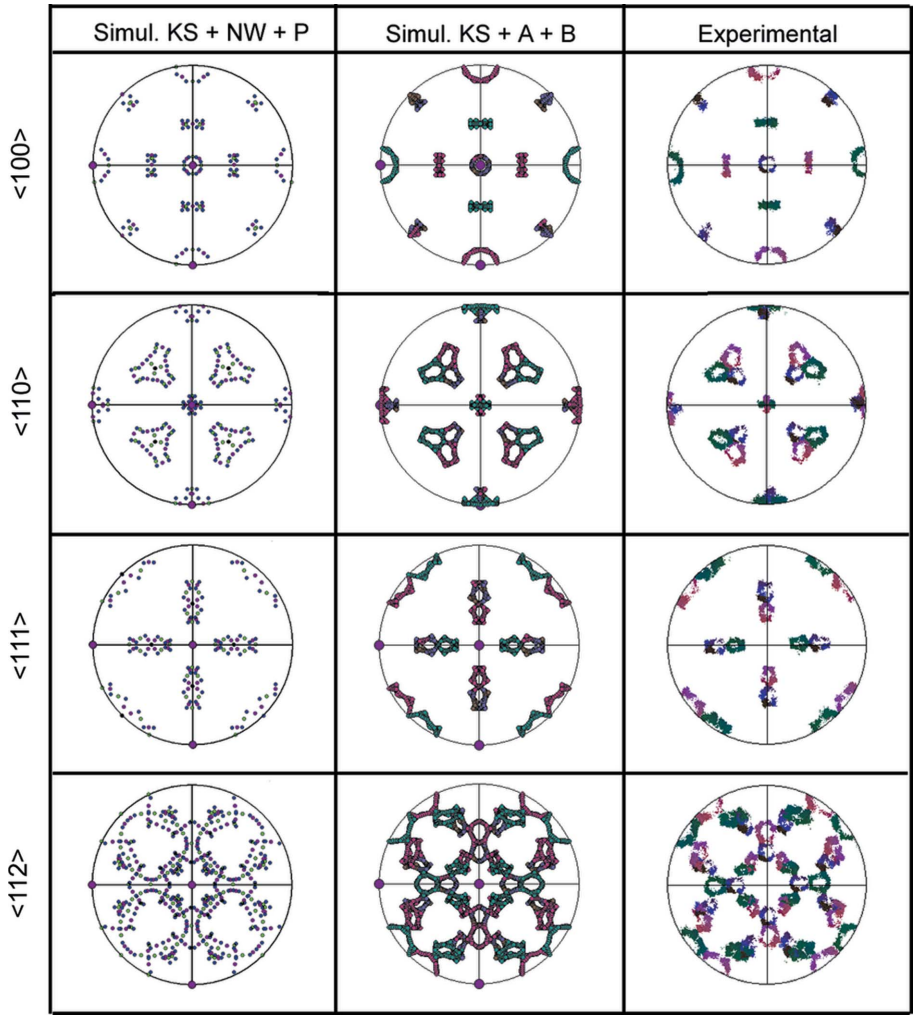

Figure 2
Pole figures of martensitic variants. First column: the 24 KS, 12 NW and 12 Pitsch variants in blue, purple and green, respectively. Second column, the 24 KS variants convoluted by the continuous rotations A(a) and B(b) with $a \in [0, 5.26^\circ]$ and $b \in [0, 5.26^\circ]$, and their composition A(c) + B(5.26° − c) with $c \in [0, 5.26^\circ]$. Third column: experimental pole figures of martensitic variants in a prior austenitic grain of a Fe-9Cr-1Mo-0.1C (EM10) steel.

This approach is quite effective for representing the crystallographic intricacy of the martensite variants. All the KS, NW and Pitsch variants are now closed on themselves by the rotations A(a) and B(b) with an angular range limited to [0, 5.26°] for both a and b, and form a structure similar to a nutshell. Is it possible to find a unique physical mechanism that could explain such a fascinating intricacy and bring information on the martensitic transformation itself? A solution is proposed in the following sections.

3. Atomic movements during Pisch distortion

The logical OR to start building a model should be the NW or KS OR, because they are the most reported ORs in steels; but they have already led to the models described in Supplementary Material 1. Could the Pitsch OR be interesting? This OR has been discovered after austenitization and the rapid

cooling of a thin TEM lamella of an iron–nitrogen alloy (Pitsch, 1959). Since the TEM thin foil is nearly in a stress-free state (or at least only under biaxial stress due to the free surface), it should be close to the OR that would be naturally obtained without the constraint imposed by the austenitic matrix in bulk materials. Moreover, as mentioned in the introduction, the Pitsch OR was reported by Sinclair (2010) and Sinclair & Hoagland (2008) from molecular-dynamics simulations.

In his paper, Pitsch transposed the OR into a tensor composed of a pure distortion and a half twin shear, without according a fundamental role to it. Let us detail here the Pitsch distortion on the atomic scale. It is assumed that during the $\gamma \rightarrow \alpha$ martensitic transformation the iron atoms are hard spheres of same diameter in both phases, which, by considering the $\langle 110\rangle_\gamma$ and $\langle 111\rangle_\alpha$ dense directions, implies that

$$\sqrt{2}a_\gamma = \sqrt{3}a_\alpha. \qquad (3)$$

The lattice parameter of pure iron extrapolated at room temperature is $a_\gamma = 0.3573$ nm, which should give $a_\alpha = 0.2917$ nm, whereas it is actually $a_\alpha = 0.2866$ nm. The difference of 2% can be attributed to the electronic and magnetic properties of iron. However, for the sake of simplicity, that difference will not be taken into consideration in the rest of this article.

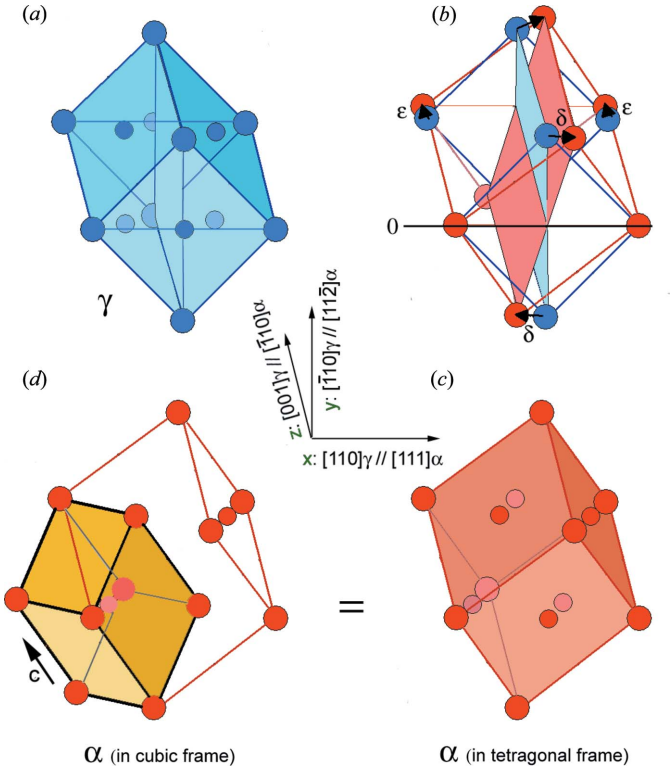

Figure 3
F.c.c.–b.c.c. transformation by Pitsch distortion in a three-dimensional representation. (*a*) F.c.c. lattice with the $(\bar{1}10)_\gamma$ plane horizontal and the $(110)_\gamma$ plane vertical; (*b*) Pitsch distortion with $x = [110]_\gamma = [111]_\alpha$ the neutral line along the horizontal direction, also marked by '0'; (*c*) b.c.c. crystal in a tetragonal frame after distortion; (*d*) the same crystal in its basic cubic reference lattice (deformed by the perspective). The Fe atoms are represented by small circles. The f.c.c. phase is in blue and the b.c.c. phase in red or orange (the same colours are used in the rest of this article).

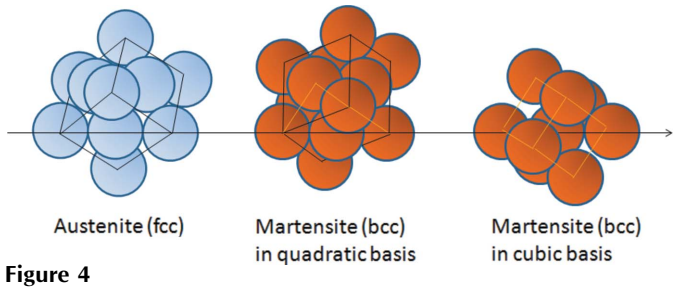

Figure 4
F.c.c.–b.c.c. transformation by Pitsch distortion with hard-sphere representation of the Fe atoms. The f.c.c. lattice and the distorted tetragonal lattice are in black, the b.c.c. lattice is in yellow. The neutral line is given by the horizontal arrow.

The Pitsch OR is $[110]_\gamma$ // $[111]_\alpha$, $[\bar{1}10]_\gamma$ // $[11\bar{2}]_\alpha$ and $[001]_\gamma$ // $[\bar{1}10]_\alpha$. These axes form an orthogonal (but not orthonormal) reference basis $B_1 = (x, y, z)$. With the hard-sphere assumption, the parallelism condition is actually the equality $[110]_\gamma = [111]_\alpha$, which means that x is a neutral (invariant) line. The initial γ lattice is shown in Fig. 3(*a*) in such a way that the $(\bar{1}10)_\gamma$ plane is horizontal and the $(110)_\gamma$ plane vertical. The distortion is represented in Fig. 3(*b*), the resulting α crystal – actually a tetragonal frame of it – is shown in Fig. 3(*c*), and its basic lattice is shown in Fig. 3(*d*). In order to make the figure easier to understand, the atoms do not have their real size, and those in the middle of faces or volumes are a little smaller than those at the corners. However, we point out that the atoms of the γ phase along the x and y axis in Fig. 3(*a*) stay in contact during the transformation along the neutral line x, and also along the y/y' directions (y for the γ phase and y' for the α phase), as represented in Fig. 4. The details in different projection views are given as follows. First, we consider the distortion of the $(001)_\gamma$ plane into the $(\bar{1}10)_\alpha$ plane, viewed along the z axis (Fig. 5*a*). The angle of 90° between the $[110]_\gamma$ and $[\bar{1}10]_\gamma$ diagonals of the $(001)_\gamma$ square is distorted into the angle of 70.5° between the $[111]_\alpha$ and $[11\bar{1}]_\alpha$ diagonals of the $(\bar{1}10)_\alpha$ rectangle. The $[110]_\gamma = [111]_\alpha$ direction remains unchanged (no dilatation and no rotation). Therefore, the distortion is completely obtained with the rotation of $y = [\bar{1}10]_\gamma$ by $\alpha = \arcsin(1/3) \simeq 19.5°$ around the common $[001]_\gamma$ // $[\bar{1}10]_\alpha$ axis, which becomes $y' = [11\bar{1}]_\alpha$, as represented by a vector δ of coordinates $\delta_x = \sin(\alpha) = 1/3$, $\delta_y = \cos(\alpha) - 1 = \sqrt{8}/3 - 1$, $\delta_z = 0$ in Fig. 3(*b*). To a rough approximation, if one assume that $\delta_y \ll \delta_x$, the distortion δ appears as a shear of value $\delta_x = 1/3$ in the $[111]_\alpha$ direction on the $(11\bar{2})_\alpha$ plane. Pitsch probably made such an approximation when mentioning a half shear of the α phase; however, all the components of δ are kept in the rest of the present article. We consider now the distortion of the $(110)_\gamma$ plane into the $(111)_\alpha$ plane, viewed perpendicularly along the x axis (Fig. 5*d*). The angle of 70.5° between the $[1\bar{1}1]_\gamma$ and $[\bar{1}11]_\gamma$ diagonals of the $(110)_\gamma$ rectangle is distorted into the angle of 60° between the $[01\bar{1}]_\alpha$ and $[10\bar{1}]_\alpha$ diagonals of the $(111)_\alpha$ triangle. The $[001]_\gamma$ direction is unrotated but transformed into the $[\bar{1}10]_\alpha$ direction by a dilatation

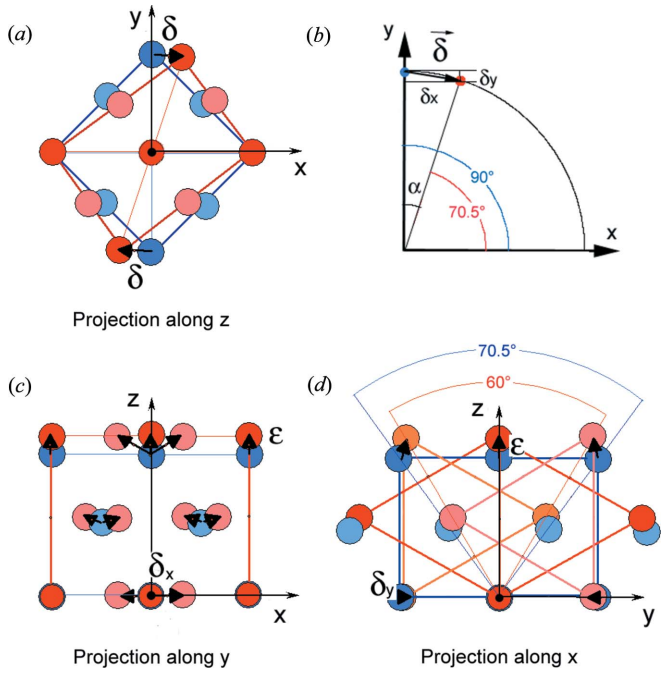

Figure 5
F.c.c.–b.c.c. transformation by Pitsch distortion viewed in projection along three axes: (*a*) and (*b*) *z* axis, (*c*) *y* axis, and (*d*) *x* axis.

of ratio $\varepsilon = 2/\sqrt{3}$ calculated from equation (3). Therefore, the Pitsch distortion matrix in the $B_1 = (x, y, z)$ basis is

$$D_{/B_1} = \begin{bmatrix} 1 & \delta_x & 0 \\ 0 & 1+\delta_y & 0 \\ 0 & 0 & \varepsilon \end{bmatrix} = \begin{bmatrix} 1 & 1/3 & 0 \\ 0 & \sqrt{8}/3 & 0 \\ 0 & 0 & 2/\sqrt{3} \end{bmatrix}. \quad (4)$$

In the reference coordinate basis B_0 (of vectors $[100]_\gamma$, $[010]_\gamma$, $[001]_\gamma$), the basis B_1 is given by the transformation matrix

$$[B_0 \rightarrow B_1] = \begin{bmatrix} 1/2 & -1/2 & 0 \\ 1/2 & 1/2 & 0 \\ 0 & 0 & 1 \end{bmatrix},$$

for which the inverse is

$$[B_1 \rightarrow B_0] = \begin{bmatrix} 1 & 1 & 0 \\ -1 & 1 & 0 \\ 0 & 0 & 1 \end{bmatrix}.$$

Therefore, the Pitsch distortion matrix in the reference coordinate basis B_0 is:

$$D_{/B_0} = [B_0 \rightarrow B_1]\, D_{/B_1}\, [B_1 \rightarrow B_0] = \begin{bmatrix} 1-\delta_b & \delta_b & 0 \\ -\delta_a & 1+\delta_a & 0 \\ 0 & 0 & \varepsilon \end{bmatrix}, \quad (5)$$

where $\delta_a = (\delta_x + \delta_y)/2$ and $\delta_b = (\delta_x - \delta_y)/2$. $D_{/B_0}$ is given numerically by

$$D_{/B_0} = \begin{bmatrix} (2+\sqrt{8})/6 & (4-\sqrt{8})/6 & 0 \\ (2-\sqrt{8})/6 & (4+\sqrt{8})/6 & 0 \\ 0 & 0 & 2/\sqrt{3} \end{bmatrix}. \quad (6)$$

The determinant of the matrix D (whatever the basis) is $\det(D) = 2(3/2)^{-3/2}$, as expected for a transformation between the b.c.c. and f.c.c. phases related by a hard-sphere model, because the theoretical ratio of the atomic volumes in the lattices is indeed $r = (a_\alpha^3/2)/(a_\gamma^3/4) = 2(3/2)^{-3/2}$, according to equation (3).

The eigenvalues of D are the real numbers $d_1 = 1$, $d_2 = \sqrt{8}/3 \simeq 0.943$ and $d_3 = \varepsilon = 2/\sqrt{3} \simeq 1.155$, associated with the normalized eigenvectors $[1/\sqrt{2}, 1/\sqrt{2}, 0]_\gamma$, $[\sqrt{2/3}, \sqrt{1/3}, 0]_\gamma$, and $[001]_\gamma$, respectively. This means that the matrix D can be diagonalized by writing it in the (not orthogonal) basis B_d formed by these vectors:

$$D_{/B_d} = \begin{bmatrix} 1/\sqrt{2} & \sqrt{2/3} & 0 \\ 1/\sqrt{2} & \sqrt{1/3} & 0 \\ 0 & 0 & 1 \end{bmatrix}^{-1} D_{/B_0} \begin{bmatrix} 1/\sqrt{2} & \sqrt{2/3} & 0 \\ 1/\sqrt{2} & \sqrt{1/3} & 0 \\ 0 & 0 & 1 \end{bmatrix} = \begin{bmatrix} 1 & 0 & 0 \\ 0 & \sqrt{8}/3 & 0 \\ 0 & 0 & 2/\sqrt{3} \end{bmatrix}. \quad (7)$$

The differences between the diagonal values and unity give the principal strain values of 0, −5.7 and +15.5%. They are lower than the −20, +12 and +12% values obtained with the Bain distortion, and even lower than with the two-step mechanism. The average of the absolute values of the principal strains is only 7.1% with the Pitsch distortion, whereas it is 10.6% with the two-step model and 14.6% with the Bain distortion. Moreover, it is worth noting that, like the Bain distortion, no shuffle (movements of atoms inside the lattice) is required in the Pitsch distortion.

4. Links between crystallographic intricacy and Pitsch distortion

From this analysis, Pitsch distortion seems to be a good candidate for explaining the f.c.c.–b.c.c. transformation. Could it be the starting point of the continuous paths observed in the pole figures, and could it explain them without other *ad hoc* parameters or mechanisms? Even if it is difficult to prove, some favourable arguments are now presented.

4.1. Pitsch distortion and the closing rotation A

Let us consider the Pitsch distortion in projection along the neutral line $x = [110]_\gamma = [111]_\alpha$ (Fig. 5*d*), and let us represent the $(110)_\gamma$ plane by an isosceles triangle and the $(111)_\alpha$ plane by an equilateral triangle. The angle of 70.5° of the $(110)_\gamma$ triangle is distorted into the angle of 60° of the $(111)_\alpha$ triangle. It can be supposed that such a distortion is principally accommodated by the γ matrix in which the α nucleus forms, as illustrated in Fig. 6. This implies that, on each face of the triangles, the f.c.c. matrix lattice is progressively rotated from 0° far from the γ/α interface to 5.26° at the two γ/α interfaces. This rotation is exactly the closing rotation A. Partial disclinations can be used to describe this rotation on the mesoscopic scale. The 60 to 70.5° distortion associated with the neutral line x can be appropriately symbolized by a wedge

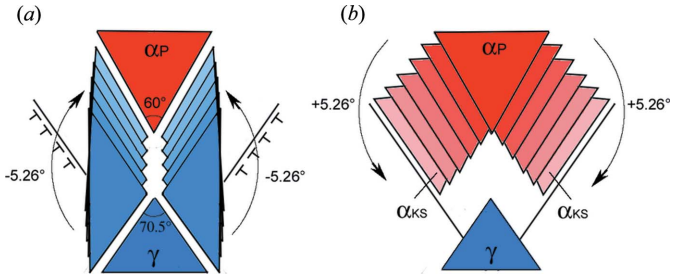

Figure 6
Explanation of the continuous rotation A (from Pitsch to KS). (*a*) Nucleation of an α_P variant (in red) by the Pitsch distortion and deformation of the γ surrounding matrix (in blue) induced by the $\gamma \rightarrow \alpha$ transformation and accommodated by dislocation pile-up which creates the progressive rotation of 10.5°/2 on each side of the α_P nucleus. (*b*) Growth of the α_P variant in the deformed γ matrix (with local Pitsch OR in the matrix). In the reference frame of austenite far from the transformation, the nucleus in Pitsch OR is progressively reoriented to two KS variants α_{KS} linked by the 2A operator.

disclination of Frank axial vector $\mathbf{w}_{2A} = (-10.5°, [110]_\gamma)$, and can be decomposed into two equal closing wedge disclinations $\mathbf{w}_A = (-5.26°, [110]_\gamma)$ on each face of the α nucleus. At the microscopic scale, the wedge disclinations could result from pile-ups on the $(\bar{1}10)_\gamma$ plane of edge sessile dislocations of line $[110]_\gamma$ and Burgers vectors $\mathbf{b} = [\bar{1}10]_\gamma$ lying on the $(001)_\gamma$ plane, as detailed in Supplementary Material 4.

After the stage of α nucleation by Pitsch distortion, the transformation continues and martensite grows by the same Pitsch mechanism. However, the surrounding γ matrix is now deformed and rotated in such a way that, even if the Pitsch OR is respected locally, the α martensite crystals are progressively rotated and reoriented globally with respect to the far austenite matrix. The rotations are those created in the γ matrix by the transformation itself during the nucleation (they are the closing rotations A on both faces of the α nucleus). At the end of the process, as shown in Fig. 6(*b*), even if Pitsch distortion is the only mechanism for both nucleation and growth, the initial nucleus variant in the Pitsch OR is reoriented during growth into two variants derived from the Pitsch nucleus by the rotation A of ±5.26°, *i.e.* into two variants in the KS OR with respect to the bulk austenite, as observed experimentally and described in §2. Of course, it prompts the question why the formation of martensite by Pitsch distortion during growth does not create another deformation field of the γ surrounding matrix to lead to an endless process and infinite rotations. Even if this question is not yet answered, we believe that the KS and NW ORs constitute locking configurations due to the parallelism of the close-packed planes.

4.2. Pitsch distortion and the closing rotation B

Is it possible to explain the closing rotation B with similar arguments? At first sight the answer is no, because none of $\{111\}_\gamma$ planes is parallel to a $\{110\}_\alpha$ plane with the Pitsch OR. Only the low-index $(001)_\gamma$ plane is transformed into the $(\bar{1}10)_\alpha$ plane (Fig. 7*a*). However, Bogers & Burgers (1964) showed that a $(\bar{1}11)_\gamma$ plane can be transformed into a $(110)_\alpha$ plane by a simple shear on a $(111)_\gamma$ plane. So, could something similar occur with the Pitsch distortion? Since we found it difficult to geometrically figure out the effect of the distortion on the $\{111\}_\gamma$ planes, the matrix $D_{/B0}$ of equation (6) has been used for calculations. For the four $\{111\}_\gamma$ planes forming a tetrahedron noted PVSQ, the image of their normal and the images of the three $\langle 110\rangle_\gamma$ edges of the triangles have been calculated. For three $\{111\}_\gamma$ planes, nothing special happens, but for the $(\bar{1}11)_\gamma$ plane the result is interesting: obviously the neutral edge $x = [110]_\gamma$ (SV) is unchanged, but the $[101]_\gamma$ and $[01\bar{1}]_\gamma$ edges become $\sim[0.80, -0.14, 1.15]_\gamma$ and $\sim[0.19, 1.14, -1.15]$ making angles of 70.5 and −54.7° with x, respectively. The image by distortion of the $(\bar{1}11)_\gamma$ normal (in reciprocal space) is calculated by using the inverse of the transpose of matrix $D_{/B_0}$ and becomes $(-1.06, -1.06, 0.86)_\gamma$, which makes an angle of 5.26° with $(\bar{1}11)_\gamma$ by a rotation around the $[110]_\gamma$ axis, *i.e.* by the rotation A. This proves that the effect of the Pitsch distortion on the $(\bar{1}11)_\gamma$ plane is: (*a*) a rotation A, which gives the intermediate KS parallelism condition, and (*b*) a distortion that transforms that plane into a $(110)_\alpha$ plane, as shown in Fig. 7(*b*) and (*c*), which is exactly the expected result. For the distortion of the $(\bar{1}11)_\gamma$ plane, the same scenario as described before for the $(110)_\gamma$ plane can be imagined. The closing rotation is now the rotation B and the associated wedge disclinations are $\mathbf{w}_B = (-5.26°, [\bar{1}11]_\gamma)$.

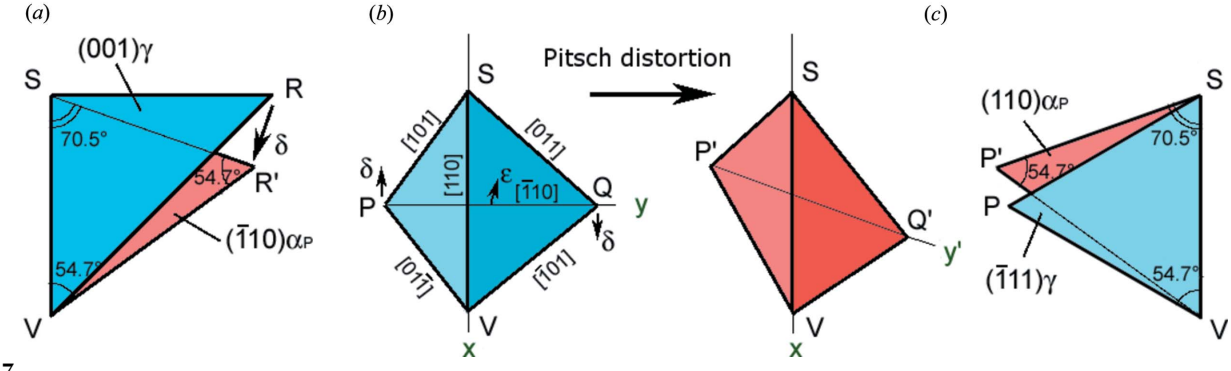

Figure 7
Effect of the Pitsch distortion on different planes: (*a*) on the $(001)_\gamma$ plane viewed in two dimensions, (*b*) on the four $\{111\}_\gamma$ planes forming the VPQS tetrahedron viewed in three dimensions, and (*c*) on the $(\bar{1}11)_\gamma$ plane. The γ planes are in blue and the α planes in red. Since SV is along the neutral line x (represented here vertically), only the corners P and Q are displaced by the Pitsch distortion and noted P′Q′.

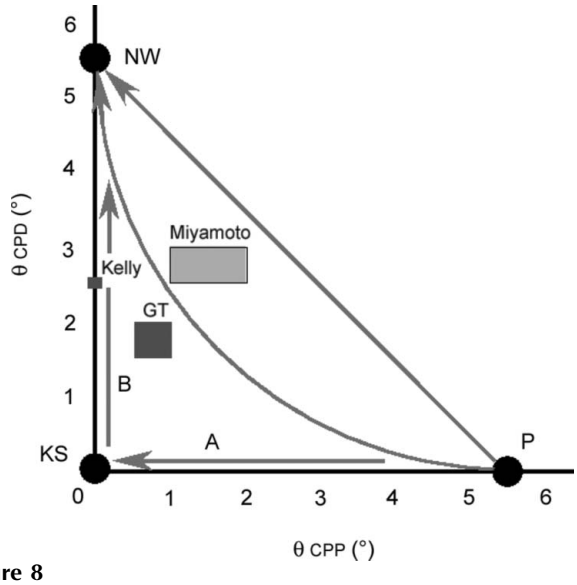

Figure 8
CPP–CPD diagram of martensitic transformation. θ_{CPP} (along the x axis) is the angular deviation between the CPPs $(111)_\gamma$ and $(110)_\alpha$, and θ_{CPD} (along the y axis) is the angular deviation between the CPDs $[110]_\gamma$ and $[111]_\alpha$. The Kelly, GT and Miyamoto ORs are also indicated. The one-step model explains the continuous path from the Pitsch OR to the KS and NW ORs by the rotations A and B.

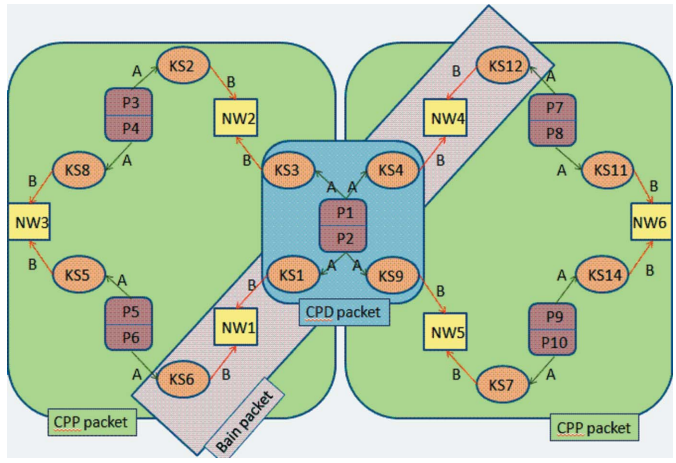

Figure 9
Schematic representation of the continuous paths between the twinned Pitsch nuclei (noted P1/P2, P3/P4 *etc.*), the intermediate KS variants obtained by rotation A, and the final NW variants obtained by rotation B. In fact, A and B result from the same Pitsch distortion and act simultaneously.

This global analysis shows that Pitsch distortion is a very good candidate for understanding: (*a*) the martensitic transformation itself and (*b*) the closed and continuous crystallographic structure formed by the NW–KS–Pitsch variants. The fascinating continuity and intricacy between the close-packed directions and planes described in §2 seem to be the natural result of only one mechanism. The α martensite nucleus is created by Pitsch distortion in the Pitsch OR inside austenite. The formation of this nucleus generates incompatibilities with the surrounding γ austenitic matrix, which are the rotational misfits 2A and 2B (accommodated by disclinations in the γ matrix). In other words, the γ matrix has been continuously rotated on each side of the α_P nucleus by the two rotations A(a) and B(b) with angles a and b varying from 0° far from the nucleus to ±5.26° close to the γ/α interface. During the martensite growth, the $\gamma \rightarrow \alpha$ transformation obeys the same Pitsch distortion, but now inside a continuously rotated γ matrix. The growth leads to new α variants misoriented from the nucleus by the 5.26° rotations A and B, *i.e.* in the KS and NW ORs with respect to the bulk austenite. These two ORs seem to act as locking configurations. In this model, the Pitsch OR appears as a precursor of the KS and NW ORs.

4.3. Schematic representation of the continuum of variant orientations

The CPP–CPD diagram introduced by Miyamoto *et al.* (2009) can be completed to represent the deviation between an OR determined experimentally and the reference KS OR, with the help of two angles: θ_{CPP}, the angular deviation between the CPPs $(111)_\gamma$ and $(110)_\alpha$, and θ_{CPD}, the angular deviation between the CPDs $[110]_\gamma$ and $[111]_\alpha$. The Pitsch OR and the transformation path with its arrow can now be added: the martensitic variants start from a Pitsch OR and are continuously reoriented toward KS (by the rotation A) and then toward NW (by the rotation B), as shown in Fig. 8. The path A followed by B, denoted (A + B), supposes that the formation mechanisms are dissociated, which is not the case, because both A and B result from the same mechanism. The structure of variants with their packets (described in Supplementary Material 3) can now be represented by using Pitsch variants as starting nuclei (grouped by twinned pairs), KS as intermediate variants, and NW as ending variants, as shown in Fig. 9. A more realistic path is a combination A × B = A(c) + B(5.26° − c) with $c \in [0, 5.26°]$, which gives the straight diagonal line from the Pitsch OR to the NW OR, or polynomial compositions, which give curves. The exact shape should depend on the mechanical properties of the austenite. The simulations presented in Fig. 2 were obtained with the A + B and A × B paths.[3] It can be noticed that the average Miyamoto OR (Miyamoto *et al.*, 2009) is close to the barycentre of the P–KS–NW triangle.

5. Revisiting the literature

5.1. Carbon content and tetragonality

The interstitial octahedral sites of austenite, *i.e.* the 12 centres of the $\langle 100 \rangle_\gamma$ edges and the centre of the lattice, which are partially occupied by carbon atoms, are transformed by Pitsch distortion into octahedral sites of the b.c.c. martensite, *i.e.* the 12 centres of the $\langle 100 \rangle_\alpha$ edges and the 6 centres of the

[3] The simulations of Fig. 2 show the continuities KS → Pitsch (rotation A) and KS → NW (rotation B), but the mechanism is actually Pitsch → KS → NW. Indeed, it was easier to use the intermediate KS as reference to draw the continuities.

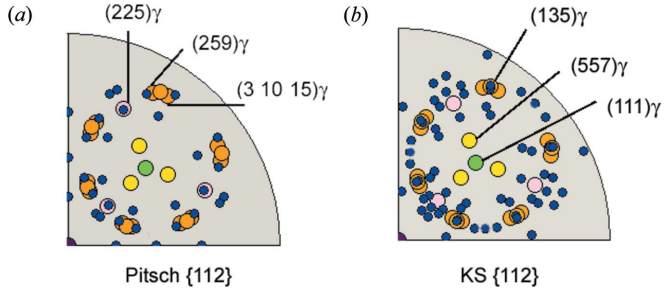

Figure 10
Stereographic projection of the habit planes of martensite reported in the literature (large circles), with (*a*) the $\{112\}_\alpha$ planes of the 12 Pitsch variants and (*b*) the $\{112\}_\alpha$ planes of the 24 KS variants (small blue discs). There is a good correspondence, except for the $(557)_\gamma$ planes.

$\{100\}_\alpha$ faces. Therefore, the Pitsch distortion could explain, as well as the Bain distortion, the fact that carbon atoms occupy the octahedral sites in the α Fe structure, despite the fact that there is less space there than in tetrahedral sites. Moreover, as in the Bain distortion, the occupation of octahedral sites may explain the tetragonal distortion of the martensite (b.c.c. $\rightarrow$ b.c.t.) along one of the $\langle 100\rangle_\alpha$ axes, which becomes the *c* axis of the b.c.t. structure at high carbon content. Indeed, with both Bain and Pitsch distortions, two $\langle 100\rangle_\alpha$ axes come from the perpendicular $[0\bar{1}1]_\gamma$ and $[01\bar{1}]_\gamma$ of the $(100)_\gamma$ plane, and the third $\langle 100\rangle_\alpha$ axis come from the $[100]_\gamma$ axis, which is therefore the natural candidate to be the *c* axis, as presented in Fig. 3(*d*).

5.2. Orientation of habit planes

The HPs were first determined in the 1930s from optical microscopy on martensite plates formed in monocrystalline austenite of known orientation (measured by X-ray diffraction), and they were, naturally, given in the reference frame of austenite. Later, in the 1950s, the HPs were determined more accurately by TEM in the austenite or martensite reference frame, but, following tradition, researchers continued reporting them in the austenite reference frame. The HPs were found to have exotic indexes such as $(225)_\gamma$, $(3,5,10)_\gamma$ *etc.* From a crystallographic point of view, trying to understand or predict HPs without understanding the mechanisms at atomic scale, as done in the PTMT, is very tricky. May the Pitsch distortion be used to understand the orientations of the HPs? For martensite in low carbon steels with needle shapes along $\langle 111\rangle_\alpha$ (Kelly & Nutting, 1960), thus without an HP, the explanation is simple: they are elongated along the neutral line $[111]_\alpha = [110]_\gamma$, which is the lowest strained direction of the transformation. To treat the other cases, the exotic HPs have been drawn in a stereographic pole figure in order to find a correspondence with the low-index planes of martensite. Different solutions have been tested and it has been found that the $\{112\}_\alpha$ planes with the Pitsch OR give very satisfactory results for the $\{225\}_\gamma$ HPs and also a quite good agreement for the $\{259\}_\gamma$ and $\{3,10,15\}_\gamma$ HPs, as shown in Fig. 10(*a*). The $\{135\}_\gamma$ HPs could also appear as $\{112\}_\alpha$ planes of martensite, but with KS OR, as shown in Fig. 10(*b*). Only the $\{557\}_\gamma$ HPs are not completely explained. Since the angle between the $(557)_\gamma$ and $(111)_\gamma$ planes is 9.4°, a link can be imagined between these planes by the rotation 2A.

The $\{225\}_\gamma$ // $\{112\}_\alpha$ HPs are in perfect agreement with the Pistch distortion because these planes contain the neutral line. In addition, it can be specified which $\{225\}_\gamma$ and $\{112\}_\alpha$ HPs in their symmetry-equivalent families are correct with respect to the $[110]_\gamma$ // $[111]_\alpha$ neutral line: they are the $(2\bar{2}5)_\gamma$ and $(\bar{2}25)_\gamma$, and the $(11\bar{2})_\alpha$, $(1\bar{2}1)_\alpha$ and $(\bar{2}11)_\alpha$ planes.

5.3. Midribs, twins and growth

Some alloys sometimes have lenticular martensite laths containing a planar zone, often in their middle, called a midrib. The formation of midribs has never been fully explained despite much research [a historical review can be found in Nishiyama (1978), pp. 43–47]. It is now agreed that the midrib is the plane of the transformation initiation, and the γ/α interface propagates laterally on either side in opposite directions. Sometimes the midrib is very sharp and can be considered as a thin plate (Shibata *et al.*, 2005, 2008). A gradual rotation inside the α crystal between the midrib and the external γ/α interfaces has been noticed (Shibata *et al.*, 2005; Jafarian *et al.*, 2011), but this observation remains unexplained. The midribs also often contain a high density of 'twins' that were promptly considered as mechanical twins associated with the 'inhomogeneous lattice-invariant' deformation required by the PTMT (Bhadeshia, 1987; Kelly & Nutting, 1960). Although this view is shared by many metallurgists, some features do not fit with it.

Let us consider for example the TEM image of Fig. 11(*a*). The 'twins' stop inside the martensite lath and do not cross it entirely. Moreover, an important detail is sometimes noticed: the boundaries of the 'twins' are generally not straight but slightly curved (Jana & Wayman, 1970; Shimizu & Nishiyama, 1972; Sandvik & Wayman, 1983), which is unusual for mechanical twins. All these features can be explained if we consider that the midrib corresponds to the nucleus Pitsch variant (α_{P1}) and that the 'twins' do not result from a mechanical shear but from the transformation itself. Indeed, in each lenticular martensite, only one 'twin' orientation is observed among the four possible Σ3 variants corresponding to the four rotations of 60° around the $\langle 111\rangle_\alpha$ directions, and we believe that this 'twin' is actually the other Pitsch variant (α_{P2}) sharing the same neutral line with the nucleus α_{P1}. The α_{P1}–α_{P2} pair of Pitsch variants results from the Pitsch distortion: the δ part of the tensor in equation (4) can be obtained in two directions deduced by inversion and, because δ is a shear in a first rough approximation, by the $(11\bar{2})_\alpha$ mirror symmetry (Fig. 5*a*). The two Pitsch variants α_{P1} and α_{P2} share the same $x = [111]_\alpha$ direction and are linked by a rotation of 60° around it. During nucleation of α_{P1}, the intricate nucleation of α_{P2} inside α_{P1} is energetically possible because both crystals share a common lattice (the Σ3 coincidence site lattice). As illustrated in Fig. 11(*b*), after nucleation the α_{P1} variant grows in a $(\bar{2}11)_\alpha$ HP, forming the midrib, and α_{P2} grows in the $(1\bar{2}1)_\alpha$ HP, which is also the mirror plane of Σ3 misorientation. The two $(\bar{2}11)_\alpha$ and $(1\bar{2}1)_\alpha$ HPs have an angle of 60°. The rotation A, gener-

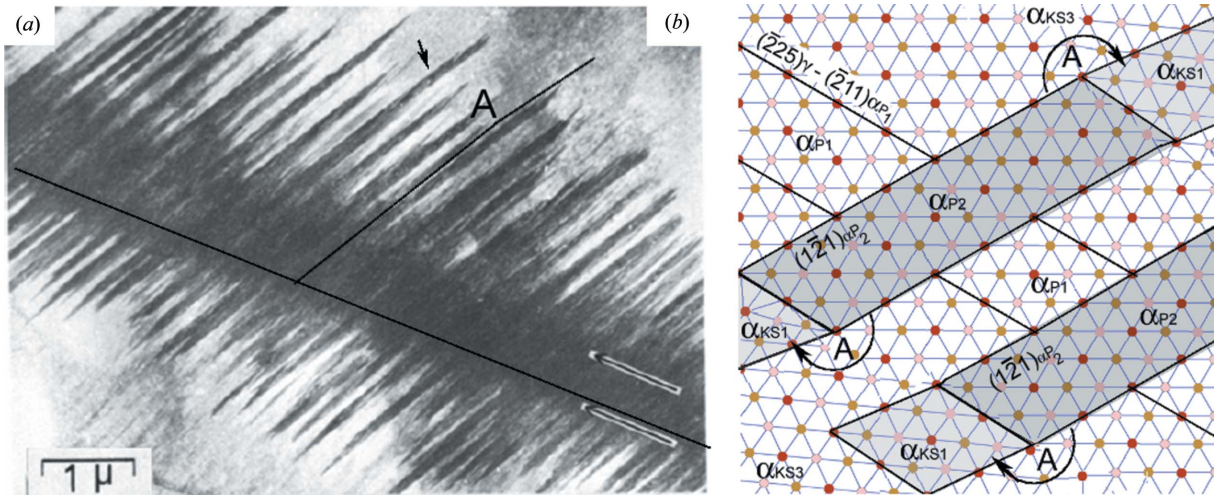

Figure 11
Midrib and 'twins' inside a lenticular martensite lath. (*a*) TEM image from Shimizu & Nishiyama (1972), reproduced with kind permission from Springer Science+Business Media B.V. The habit planes of the 'twins' make an angle of 60° with the midrib and they are curved at the mark 'A', also visible at the arrow tip. The surrounding austenite is not visible. (*b*) Schematic representation with the lattices. The 'twins' can be considered as Pitsch variants α_2 in twin orientation relationship with the main Pitsch variant α_1 forming the midrib. The HPs of both variants are $\{112\}_\alpha$ planes and the curvature agrees with the rotation A, which results from the deformation of the surrounding matrix during the formation of the nucleus α_1.

ated by the deformation field of the Pitsch distortion (§4.1), acts differently on the α_{P1} and α_{P2} variants because of the difference of orientations and HPs. The α_{P1} midrib continues to grow laterally and its lattice is gradually rotated so that its orientation gets close to KS: α_{P1} has been transformed progressively into the α_{KS3} variant according to the scheme of Fig. 9. The martensite lath acquires a lenticular shape, often asymmetric due to the rotation A. The α_{P2} 'twins' continue to grow; the rotation A transforms them progressively into an α_{KS1} variant, and also curves the $(1\bar{2}1)_\alpha$ boundary. This 5.26° curvature, marked by the broken line A in Fig. 11(*a*), creates additional strains with the surrounding α_{P1} crystal, which stops the growth process, as represented in Fig. 11(*b*). The α_{P1}, α_{P2}, α_{KS3} and α_{KS1} variants belong to the same CPD packet.

5.4. Butterfly martensite

Among the wide variety of shapes and morphologies, butterfly martensite is probably the most intriguing. It is formed by two lenticular-shaped wings in two distinct $\{225\}_\gamma$ planes and, as a lenticular martensite, it can present the same internal features, such as a midrib, 'twins', $(110)_\alpha$ planar faults and serrations (Umemoto *et al.*, 1984; Gong, 1987; Zhang *et al.*, 1993).

Sato & Zaefferer (2009) and Sato *et al.* (2009) showed recently by EBSD that the α lattice inside a wing is gradually deformed by a rotation around the common $[111]_\alpha = [110]_\gamma$ axis with a maximum angle generally between 5 and 10°, *i.e.* by the rotation A. There is another interesting point that can be noticed in the EBSD map reported in Fig. 12(*a*): the two wings have the same orientation and the same internal gradient of orientations despite their different HPs. This may be explained by the butterfly having been nucleated first at the point noted '0', which is the intersection of two glide planes forming one Pitsch variant. The $(002)_\gamma$ // $(\bar{1}10)_\alpha$ mirror symmetry of the austenite-Pitsch variant system makes the growth on the two $(\bar{2}25)_\gamma$ // $(\bar{2}11)_\alpha$ and $(2\bar{2}5)_\gamma$ // $(1\bar{2}1)_\alpha$ HPs equivalent and explains the presence of two wings for a unique Pitsch nucleus. Moreover, in the butterfly martensite of Fig. 12(*a*) there is no midrib, which means that the growth occurs only towards the inner direction and both wings are continuously rotated by the same rotation A whatever the HP is. The growth stops when the $(01\bar{1})_\alpha$ planes become parallel to $(1\bar{1}1)_\gamma$. The case studied here corresponds to a monocrystalline butterfly martensite in which the two $(\bar{2}25)_\gamma$ and $(2\bar{2}5)_\gamma$ HPs intersect at the neutral line $[111]_\alpha = [110]_\gamma$. The angle of the two wings is 58.99°. As reported in the literature, it seems that there are many other configurations for the pairs of $\{225\}_\gamma$ HPs with angles ranging from 41 to 139° (Gong, 1987). We believe that systematic precise EBSD studies on the pairs of wings could help to better understand these cases.

5.5. Effect of a prior plastic deformation of austenite

It has been acknowledged for a long time that the plastic deformation of austenite before quenching increases the martensite start (MS) temperature, which means that a prior plastic deformation favours the martensite formation. This strain-induced nucleation of martensite has been clearly shown to involve shear systems of austenite such as stacking faults or ε plates (Olson & Cohen, 1972). We think that this fact can be explained with the one-step theory. The intersection line of the two shear or glide bands is indeed the place of very high strain concentrations that help to distort the angle of 70.5° of the $(110)_\gamma$ plane into the angle of 60° of the $(111)_\alpha$ plane, as described in §4.1. The shear intersections could act as Lomer–Cottrell locks and sources of wedge disclinations that would reduce the energy barrier between the γ and α phases,

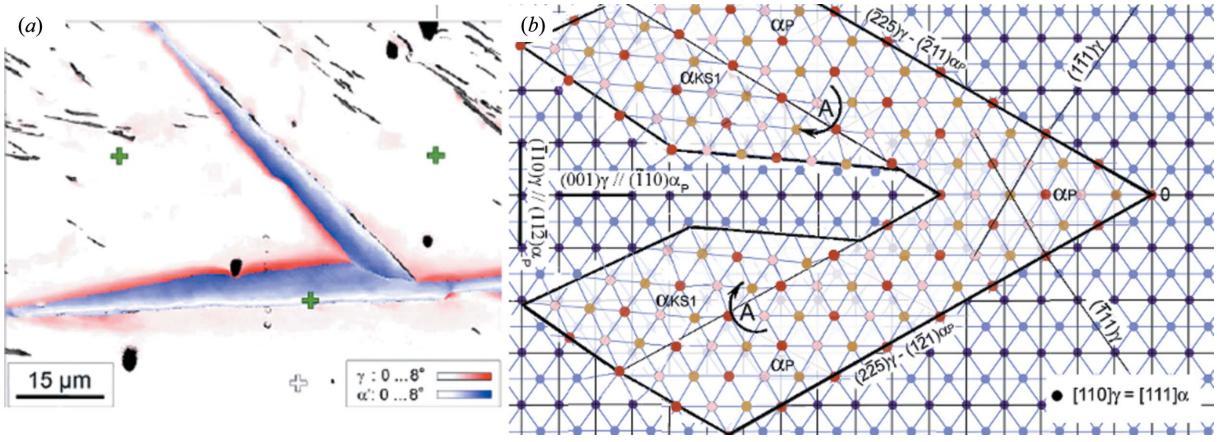

Figure 12
Butterfly martensite. (*a*) EBSD map showing the misorientations inside the martensite and in the austenite matrix [reprinted from Sato & Zaefferer (2009) with permission from Elsevier]. The red/blue colours are inverted with respect to our paper. (*b*) Schematic presentation with the lattices of the phases. Nucleation of a martensite variant in Pitsch OR at point noted '0', and growth, first along the $\{112\}_\alpha$ planes and later by the thickening of the wings with the gradual rotation A, are shown. The angle between the planes $(2\bar{2}5)_\gamma$ and $(\bar{2}25)_\gamma$ is 58.99° and the angle between $(11\bar{2})_\alpha$ and $(2\bar{1}1)_\alpha$ is 60°.

and therefore trigger the martensite nucleation. This case is illustrated by using the TEM images of Shimizu & Nishiyama (1972), as detailed in Supplementary Material 5*a*.

The one-step theory predicts that the intersection line is the $\langle 110\rangle_\gamma$ neutral line of the Pitsch distortion, and the variants are grouped by packets as follows: two variants with Pitsch OR (in quenched thin TEM samples, for example), four variants with KS OR, and four variants with NW OR. Examples of packets are P1 + P2, KS1 + KS3 + KS4 + KS9 and NW1 + NW2 + NW4 + NW5, illustrated in Fig. 9. Bokros & Parker (1963) showed that plastic strains prior to martensite transformation promote the formation of clusters of four variants about common $\langle 110\rangle_\gamma$ directions. Similarly, Gong *et al.* (2013) recently reported that bainitic transformation is accelerated by ausforming, which is associated again with a strong variant selection. They showed by EBSD that the bainitic laths are in NW OR and are grouped by packets of four variants. The authors explained this with Bain strains and Shockley partial dislocations. Actually, these packets are exactly those predicted by the one-step theory, as detailed in Supplementary Material 5*b*.

5.6. Internal and edge defects

The many $(110)_\alpha$ // $(111)_\gamma$ planar defects observed in lenticular martensite by Jana & Wayman (1970), Shimizu & Nishiyama (1972), Sandvik & Wayman (1983) and in butterfly martensite by Umemoto *et al.* (1984), Gong (1987) and Zhang *et al.* (1993) might be explained as follows: the deformation of austenite in the surrounding of a nucleated martensite is accommodated by the disclinations A constituted by dislocations on a specific $(111)_\gamma$ plane (§4.1 and Supplementary Material 5). When the austenite is in turn transformed into martensite with local Pitsch OR, the $(111)_\gamma$ planar defects are probably transformed into $(110)_\alpha$ defects by 'inheritance'. Similarly, the many sets of parallel screw dislocations with Burgers vector $\frac{1}{2}[111]_\alpha$ // $\frac{1}{2}[110]_\gamma$ observed by Sandvik & Wayman (1983) could result from the accommodating disclinations w_B (§4.2) and an inheritance mechanism during the martensitic transformation.

The origin of serrations, which are small notches sometimes visible on the edge of martensite (Jana & Wayman, 1970; Maki *et al.*, 1973) is still not well understood. Jana & Wayman (1970) consider that 'The serrations can correspond to the termination of growth in local sections of the plates due to constraints in the matrix, or to the nucleation of side plates of other habit plane variants', but this seems contradictory. It can easily be understood that the $(111)_\gamma$ planar defects act as barriers and block the martensite growth, but the fact that they could help the nucleation is more difficult to explain. In the one-step theory, since the intersection of two glide planes can trigger the martensite Pitsch distortion, the striations can be conceived of as regeneration sources of the martensite growth and the dislocations on the $(111)_\gamma$ planar defects could feed the disclinations necessary to the martensite transformation. These defects could stop the growth of the martensite plates for a short instant and, once the intersection points are filled enough with dislocations to create the disclination, the martensite would grow again in its main HP, or in another $(225)_\gamma$ HP, as in butterfly martensite.

6. Conclusions

A theory of $\gamma \rightarrow \alpha$ martensitic transformation based on Pitsch distortion is proposed to explain the crystallographic intricacy and the continuous orientations of martensite variants visible in the EBSD pole figures.

The Pitsch distortion respects the hard-sphere packing of the iron atoms. It consists of a distortion of the $(110)_\gamma$ plane into the $(111)_\alpha$ plane (explaining the rotation A), followed by a distortion of the $(\bar{1}11)_\gamma$ plane into the $(110)_\alpha$ plane (explaining the rotation B). There is a neutral line along the close-packed direction $[110]_\gamma = [111]_\alpha$ and no shuffle is required. The Pitsch distortion can be expressed by a simple

diagonal matrix (in a non-orthogonal reference frame) with principal strains of 0, −5.7 and 15.5%, therefore well below the +12, +12, −20% values of the Bain distortion. During nucleation, the surrounding austenite matrix is deformed to accommodate the Pitsch distortion. During growth, the martensite continues to form by the Pitsch distortion inside the deformed matrix, and thus it is gradually misoriented by the rotations of angles ranging from 0 to 5.26° around the $[110]_\gamma$ and $[\bar{1}11]_\gamma$ directions, on each side of the nucleus, to finally end with KS and NW ORs with respect to the matrix, far from the nucleus. The continuous rotations inside the martensite variants, and the KS and NW ORs, all result from the Pitsch distortion and the gradual reorientation of the variants during their growth in the deformation field of the surrounding austenitic matrix created by the transformation itself.

This model can be used to reinterprete some microstructural features reported in the literature. Most of the time, the elongated direction of the martensite, whatever its shape (needles, lath or lenticular plates), contains the $[110]_\gamma$ neutral line. The $\{225\}_\gamma$ habit planes correspond to low-index $\{112\}_\alpha$ facets of the Pitsch martensite nucleus. The 'twins' sometimes observed at the midrib are Pitsch variants created by the phase transformation itself. The effect of prior plastic deformation of austenite can be explained by the creation of an intersection $\langle 110\rangle_\gamma$ line between two $\{111\}_\gamma$ glide planes with a distortion field that triggers the Pitsch distortion during cooling and thus the martensitic transformation. This process could explain the variant selection which results from ausforming, and the serration sometimes observed at the edge of the lenticular martensite.

We consider that the main ideas of the theory also apply to bainitic transformations, since the one-step model is based on the continuous features observed in the EBSD pole figures, and the features in martensite and bainite are similar.

7. Related literature

Some crystallographic models of martensitic transformation are discussed in Bain (1924), Shimizu & Tanaka (1978), Kurdjumow & Sachs (1930), Nishiyama (1934, 1978), Greninger & Troiano (1949), Kelly & Groves (1973), Bogers & Burgers (1964), Olson & Cohen (1972, 1976), Wechsler *et al.* (1953), Bowles & Mackenzie (1954), Bhadeshia (1987), Christian (2002), Acton & Bevis (1969) and Zhang & Kelly (2009). For the effect of the EBSD step size on the pole figures of martensitic variants, see Cayron (2007*a*) and Nolze (2004). On the use of a groupoid composition table to define crystallographic packets of martensitic variants in the KS OR, see Gourgues *et al.* (2000), Lambert-Perlade *et al.* (2004), Morito *et al.* (2003, 2006), Cayron (2006, 2007*b*) and Cayron *et al.* (2006). Pitsch rotations A and B, disinclinations and dislocations are discussed in Volterra (1907), Romanov (2003), Kleman & Friedel (2008), Klimanek *et al.* (2001), Murayama *et al.* (2002), Lomer (1951), Cottrell (1952), Kajiwara *et al.* (1996), Ogawa & Kajiwara (2007), Shibata *et al.* (2010) and Pond *et al.* (2008). On the effect of plastic deformation of austenite see Olson & Cohen (1972), Shimizu & Nishiyama (1972), Nishiyama (1978), Sandvik & Wayman (1983), Gong *et al.* (2013) and Cayron (2007*a*). Figs. S1_2, S1_3, S1_4 and S5_2 are reprinted with permission from Elsevier, and Fig. S1_1 is reproduced with kind permission from Springer Science+ Business Media B.V.

CC would like to thank the reviewers for their advice; Samantha Zapata for her help with the English; and Stephan Zaefferer, Goro Miyamoto, Hisashi Sato, Yves Bréchet, Muriel Véron, Laure Guétaz, Pasi Suikkanen, Yann de Carlan and Eric Payton for discussions about EBSD and martensite.

References

Acton, A. & Bevis, M. (1969). *Mater. Sci. Eng.* **5**, 19–29.
Bain, E. C. (1924). *Trans. Am. Inst. Min. Metall. Eng.* **70**, 25–35.
Bhadeshia, H. K. D. H. (1987). *Worked Examples in the Geometry of Crystals*, 2nd ed. Brookfield: The Institute of Metals.
Bogers, A. & Burgers, W. (1964). *Acta Metall.* **12**, 255–261.
Bokros, J. & Parker, E. (1963). *Acta Metall.* **11**, 1291–1301.
Bowles, J. & Mackenzie, J. (1954). *Acta Metall.* **2**, 129–137.
Cayron, C. (2006). *Acta Cryst.* A**62**, 21–40.
Cayron, C. (2007*a*). *J. Appl. Cryst.* **40**, 1179–1182.
Cayron, C. (2007*b*). *J. Appl. Cryst.* **40**, 1183–1188.
Cayron, C., Artaud, B. & Briottet, L. (2006). *Mater. Charact.* **57**, 386–401.
Cayron, C., Barcelo, F. & de Carlan, Y. (2010). *Acta Mater.* **58**, 1395–1402.
Christian, J. W. (2002). *The Theory of Transformations in Metals and Alloys*, Part II, pp 961–1113. Oxford: Elsevier Science Ltd.
Cottrell, A. H. (1952). *Philos. Mag.* **43**, 645–647.
Dahmen, U. (1982). *Acta Metall.* **30**, 63–73.
Gong, H. (1987). *Metallography*, **20**, 263–275.
Gong, W., Tomota, Y., Adachi, Y., Paradowska, A., Kelleher, J. & Zhang, S. (2013). *Acta Mater.* **61**, 4142–4154.
Gourgues, A. F., Flower, H. M. & Lindley, T. C. (2000). *Mater. Sci. Technol.* **16**, 26–40.
Greninger, A. B. & Troiano, A. R. (1949). *J. Met. Trans.* **185**, 590–598.
Jafarian, H. R., Borhani, E., Shibata, A., Terada, D. & Tsuji, N. (2011). *J. Mater. Sci.* **46**, 4216–4220.
Jana, S. & Wayman, M. (1970). *Metall. Trans.* **1**, 2825–2832.
Kajiwara, S., Ogawa, K. & Kikuchi, T. (1996). *Philos. Mag. Lett.* **74**, 405–414.
Kelly, A. & Groves, G. W. (1973). *Crystallography and Crystal Defects*, pp. 313–338. London: Longman Group Ltd.
Kelly, P. M. & Nutting, J. (1960). *Proc. R. Soc. London*, **259**, 45–58.
Kleman, M. & Friedel, J. (2008). *Rev. Mod. Phys.* **80**, 61–115.
Klimanek, P., Klemm, V., Romanov, A. E. & Seefeldt, M. (2001). *Adv. Eng. Mater.* **3**, 877.
Kurdjumow, G. & Sachs, G. (1930). *Z. Phys.* **64**, 325–343.
Lambert-Perlade, A., Gourgues, A. & Pineau, A. (2004). *Acta Mater.* **52**, 2337–2348.
Lomer, W. M. (1951). *Philos. Mag.* **42**, 1327–1331.
Maki, T., Shimooka, S., Arimoto, T. & Tamura, I. (1973). *Trans. JIM*, **14**, 62–67.
Miyamoto, G., Shibata, A., Maki, T. & Furuhara, T. (2009). *Acta Mater.* **57**, 1120–1131.
Morito, S., Huang, X., Furuhara, T., Maki, T. & Hansen, N. (2006). *Acta Mater.* **54**, 5323–5331.
Morito, S., Tanaka, H., Konishi, R., Furuhara, T. & Maki, T. (2003). *Acta Mater.* **51**, 1789–1799.
Murayama, M., Howe, J. M., Hidaka, H. & Takaki, S. (2002). *Science*, **295**, 2433–2435.
Nishiyama, Z. (1934). *Sci. Rep. Tohoku Imp. Univ.* **23**, 637–644.

Nishiyama, Z. (1978). *Martensitic Transformation*, edited by M. E. Fine, M. Meshii & C. M. Waymann. Materials Science Series. New York: Academic Press.
Nolze, G. (2004). *Cryst. Res. Technol.* **39**, 352–353.
Ogawa, K. & Kajiwara, S. (2007). *Mater. Trans.* **48**, 860–868.
Olson, G. & Cohen, M. (1972). *J. Less-Common Met.* **28**, 107–118.
Olson, G. B. & Cohen, M. (1976). *Metall. Trans*, **7**, 1905–1914.
Pitsch, W. (1959). *Philos. Mag*, **4**, 577–584.
Pond, R. C., Ma, X. & Hirth, J. P. (2008). *J. Mater. Sci.* **43**, 3881–3888.
Romanov, A. (2003). *Eur. J. Mech. A Solids*, **22**, 727–741.
Sandoval, L., Urbassek, H. M. & Entel, P. (2009). *New J. Phys.* **11**, 103027.
Sandvik, B. P. J. & Wayman, C. M. (1983). *Metall. Trans.* **14A**, 2455–2477.
Sato, H. & Zaefferer, S. (2009). *Acta Mater.* **57**, 1931–1937.
Sato, H., Zaefferer, S. & Watanabe, Y. (2009). *ISIJ Int.* **49**, 1784–1791.
Shibata, A., Furuhara, T. & Maki, T. (2010). *Acta Mater.* **58**, 3477–3492.
Shibata, A., Morito, S., Furuhara, T. & Maki, T. (2005). *Scr. Mater.* **53**, 597–602.
Shibata, A., Murakami, T., Morito, S., Furuhara, T. & Maki, T. (2008). *Mater. Trans.* **49**, 1242–1248.
Shimizu, K. & Nishiyama, Z. (1972). *Met. Trans.* **3**, 1055–1068.
Shimizu, K. & Tanaka, Y. (1978). *Trans. JIM*, **19**, 685–693.
Sinclair, C. W. (2010). *J. Phys. Conf. Ser.* **240**, 012105.
Sinclair, C. & Hoagland, R. (2008). *Acta Mater.* **56**, 4160–4171.
Umemoto, M., Hyodo, T., Maeda, T. & Tamura, I. (1984). *Acta Metall.* **32**, 1191–1203.
Volterra, V. (1907). *Ann. Ec. Norm. Sup. Paris*, **24**, 401–518.
Wassermann, G. (1933). *Arch. Eisenhüttenwes.* **6**, 347–351.
Wechsler, M. S., Lieberman, D. S. & Read, T. A. (1953). *Trans. Am. Inst. Min. Metall. Eng.* **197**, 1503–1515.
Zhang, M. & Kelly, P. M. (2009). *Prog. Mater. Sci.* **54**, 1101–1170.
Zhang, X., Li, D., Xing, Z., Gautier, E., Zhang, J. & Simon, A. (1993). *Acta Metall. Mater.* **41**, 1693–1699.